RSC Advances

ROYAL SOCIETY OF CHEMISTRY

www.rsc.org/advances

Cite this: DOI: 10.1039/c0xx00000x

www.rsc.org/xxxxxx

ARTICLE TYPE

Biotemplated Synthesis of Hierarchically Nanostructured TiO_2 Using Cellulose and Their Applications in Photocatalysis

Tianrui Chen, Yu Wang*, Yun Wang, Yan Xu*

Received (in XXX, XXX) Xth XXXXXXXXX 20XX, Accepted Xth XXXXXXXXX 20XX

DOI: 10.1039/b000000x

Hierarchically nanostructured TiO_2 have been hydrothermally synthesized using cellulose as biotemplate involving various types of acids. We show that the surface charges of nanocrystalline cellulose and reaction parameters including reaction temperature, acid to cellulose ratio and reaction time have strong effect on the morphology and nanostructures of TiO_2 products. The photocatalytic activity of as-synthesized, calcined hierarchically nanostructured TiO_2 and calcined hierarchically nanostructured TiO_2 loaded Au nanoparticles is evaluated by photo-degradation of methyl orange under white light.

INTRODUCTION

Photocatalysis using sunlight has attracted considerable attention worldwide due to the increasing demand for environmental remediation and energy conservation.[1-3] Since 1972, TiO_2 has been extensively studied for applications in environmental cleaning, hydrogen energy and solar cells owing to its favourable photocatalytic activity, nontoxic nature and chemical inertness.[4-10] Unfortunately, large scale market adoption of TiO_2 photocatalyst is challenged by its low photo-conversion efficiency.[11] Numerous efforts have been devoted to design and fabricate hierarchically nanostructured TiO_2 and TiO_2 with tailored Facets to achieve improved performance.[12-20] Among them, bio-templated synthesis of TiO_2 holds exciting implications for creating hierarchical nanostructures.[21-26]

Cellulose is the most abundant biopolymer on earth.[27-28] It is a linear polysaccharide based on β-1,4-linked D-glucose units and contains large quantity of active hydroxyl groups. Cellulose chains are aggregated through intra-and inter-molecular hydrogen-bonded network and lead to various polymorphs.[29, 30] Native cellulose consists of noncrystalline and crystalline domains, and nanocrystalline cellulose (NCC) can be recovered from native cellulose using acid hydrolysis.[31-35] Literatures show that cellulose can be acid hydrolyzed to water insoluble and soluble oligomers and to glucose under hydrothermal conditions.[35] Thus, it is worth exploring the hydrothermal synthesis of hierarchically nanostructured TiO_2 by using cellulose as biotemplate under different acidic conditions.

In the present work, various hierarchically nanostructured TiO_2 have been hydrothermally synthesized in the presence of microcrystalline cellulose (MCC) and different types of acids including sulfuric acid (H_2SO_4) and hydrochloric acid (HCl). The experimental parameters, including the type of acid, reaction temperature, acid-to-cellulose ratio and reaction time, are found having strong effect on the morphology and structure of the products, which may be due to the surface properties of NCC functionalized during crystallization. The photocatalytic activity of as-synthesized hierarchically nanostructured TiO_2 (HNT), calcined hierarchically nanostructured TiO_2 (CHNT) and calcined hierarchically nanostructured TiO_2 loaded Au nanoparticles (CHNT@Au) is evaluated for the degradation of methyl orange (MO) under white light.

EXPERIMENTAL SECTION

Materials

All chemicals were purchased and used without further purification. Titanium tetrafluoride (TiF_4) was purchased from Baiao chemical company. MCC was purchased from Sigma-Aldrich. Hydrogen tetrachloroaurate (III) trihydrate ($HAuCl_4$, ACS, 99.99%) was purchased from Alfa Aesar. H_2SO_4 (98%), HCl (37%) were purchased from Beijing chemical company.

Preparation of HNT and CHNT

In a typical experiment, 0.025 g of MCC was added to 5 mL of deionized water at atmosphere condition, followed by the addition of 5 mL (0.04 mM) of TiF_4 aqueous solution. Next, stoichiometric amount of acid each was added to the above solution and stirred for 2h until homogenous mixtures were obtained. It was then sealed in Teflon-lined stainless steel autoclaves and heated at different temperature for 24h under static conditions, and cooled to room temperature in ambient atmosphere. The as-synthesized TiO_2 products were recovered by centrifugation and washed three times with ethanol to remove the organic residues. The products were dried in air for 24h at 60°C. The as-synthesized TiO_2 products were calcined to remove the carbon coating at 550°C for 2h in a muffle furnace at a heating rate of 1 °C/min to form the CHNT products. The preparation of CHNT@Au can be found in the electronic supplementary information (ESI).

Characterization

The surface morphology of as-prepared TiO_2 products was analyzed by a JEOL-6700F field emission scanning electron microscope (FE-SEM) at an accelerating voltage of 3kV. The structural property of the samples was measured with a Rigaku D/Max 2550 X-ray diffractometer (XRD) using a monochromatized Cu target radiation resource (λ = 1.54 Å). The detailed microstructure of the TiO_2 and TiO_2@Au products was analyzed by using a FEI Tecnai G-2S-Twin transmission electron microscope (TEM) with a field emission gun operating at 200kV. The X-ray photoelectron spectra (XPS) was measured by ESCALab 250 Analytical XPS spectrometer with a monochromatic X-ray source (Al KR, h=1486.6 eV). UV-vis absorption (UV) spectra were performed by a SHIMADZU UV-2450 spectrometer. Thermal gravimetric analysis (TGA) was carried out using a NETZSCH STA 449 C instruments under air from 300 K to 1173 K.

Photocatalytic Activity

The photocatalytic activity of as-synthesized HNT, CHNT and CHNT@Au products was investigated by MO degradation (20 mg/L) under white light. In a typical experiment, 20 mg HNTs or CHNTs or CHNT@Au were added to 50 mL (20 mg/L) MO dye solution and mixed under magnetic stirring for at least 2h in darkness to establish an adsorption/desorption equilibrium at room temperature, prior to exposure to light source. In photocatalytic assessments, the distance between the light source and cuvette was 10 cm. The solution was under magnetic stirring during the entire experimental procedure. The photocatalytic activities were quantified by collecting the UV-vis absorption spectra of the solution at different reaction intervals.

RESULT AND DISCUSSION

Crystal Morphology

Hierarchically nanostructured TiO_2 (HNTs) crystals were hydrothermally synthesized from the reaction systems containing H_2SO_4 and different molar ratio of H_2SO_4/MCC at 140°C-180°C for 24h, designated as HNT-Sn (n=1-6). Specifically, HNT-S1 was obtained from the reaction mixture containing H_2SO_4/MCC ratio of 171 (according to the molecular weight of the monomer of cellulose) at 140°C. The crystals of HNT-S1 have uniform shape with rugged surface based on FE-SEM images (Fig. 1a). Increasing reaction temperature from 140°C to 160°C results in the formation of HNT-S2 showing smoother surface and more regular crystal shapes compared to HNT-S1 (Fig. 1b). Increasing reaction temperature further to 180°C, HNT-S3 with even smoother surface compared to HNT-S2 and some well-defined crystal facets was obtained (Fig 1c). In parallel, the detailedly evolutionary crystallization of HNTs was investigated by varying the H_2SO_4 amount of the reaction mixture and keeping the crystallization at 140°C for 24h, as shown in Fig S1-6. These experimental results indicate that the low H_2SO_4 amount induces the formation of spherical morphology of hierarchical TiO_2 nanostructures with a lot of NCC in the reaction system and high H_2SO_4 amount induces the formation of flattened morphology of hierarchical TiO_2 nanostructures without NCC in the reaction system. Especially, HNT-S4 was obtained from the reaction mixture containing the H_2SO_4/MCC ratio of 712 after 24h at 140°C (Fig. 1d). It has flattened crystal shape and carved surface

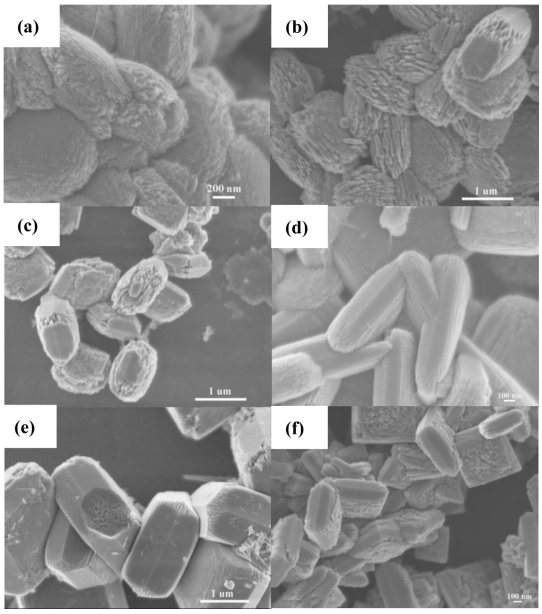

Fig.1 FE-SEM images of the hierarchical nanostructured TiO_2 (HNT-Sn) by varying the reaction temperature and the amounts of H_2SO_4 and MCC: (a) HNT-S1; (b) HNT-S2; (c) HNT-S3; (d) HNT-S4; (e) HNT-S5; (f) HNT-S6.

texture compared to HNT-S1. HNT-S5 and HNT-S6 were obtained from reaction mixtures containing the H_2SO_4/MCC ratio of 758 after 24h at 160°C and 180°C, respectively. It is intriguing to note that the crystal of HNT-S5 consists of bundles of nanocrystalline plates with very smooth crystal surface (Fig. 1e). The surface texture of HNT-S6 differs from any of the above (Fig. 1f). Parallel experiments show the similar results when reaction temperature changes from140°C to 160°C and 180°C, while keep other reaction parameters constant. The results suggest that reaction temperature and H_2SO_4/MCC ratio play critical role in controlling the crystal morphology of HNT-Sn. High amount of H_2SO_4 is helpful to form smoother surface compared to low amount of H_2SO_4.

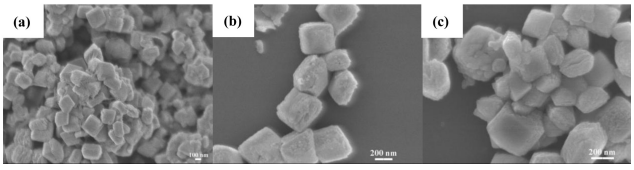

Fig.2 FE-SEM images of the ab-obtained hierarchically nanostructured TiO_2 (HNT-Cn) by varying the reaction temperature and remaining the amounts of HCl and MCC: (a) HNT-C1; (b) HNT-C2; (c) HNT-C3.

The crystal morphology of HNTs obtained from reaction mixtures containing varying HCl/MCC ratios in the temperature range of 140°C to 180°C, named as HNT-Cn (n=1-3) was studied using FE-SEM as shown in Fig. 2. HNT-C1, C2 and C3 obtained from the reaction mixtures containing HCl/MCC ratio of 495 at 140°C, 160°C and 180°C, respectively, have similar crystal shapes and coarse surface texture. In parallel, the detailedly evolutionary crystallization of TiO_2 was investigated by varying the HCl amount of the reaction mixture, while keeping the

crystallization at 140°C for 24h, as shown in Fig S7-9. The results indicate that the morphology does not obviously change. However, the yield increases with increasing the HCl amount. Further increase the HCl amount to 2.0 mL results in a change in crystal morphology, *i.e.*, crystal becoming flattened and surface texture being rougher (Fig. S10a-b). Increasing the crystallization temperature results in smoother surfaces and more regular crystal shapes, specifically, the tetragonal bipyramid and spherical crystals obtained from crystallization at 160°C and 180°C, respectively (Fig. S10c-f). Decreasing the HCl/MCC ratio results in the formation of spherical shape (Fig. S11). We conclude that the crystal morphology and surface of HNT-Cn is also affected by crystallization temperatures and the HCl/MCC ratios. However, the H_2SO_4 have more effect on the crystallization of HNT than HCl.

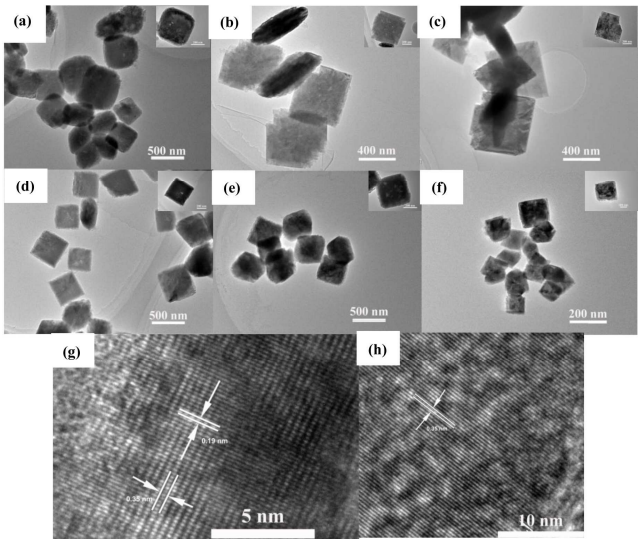

Fig.3 TEM and HRTEM images of the HNT-Sn and HNT-Cn (a) TEM image of HNT-S1; (b) TEM image of HNT-S2; (c) TEM image of HNT-S3; (d) TEM image of the HNT-C1; (e) TEM image of the HNT-C2; (f) TEM image of HNT-C3; (g) HRTEM image of HNT-S1; (h) HRTEM image of HNT-C1. Insets show the magnified TEM images of the respective single nanostructures.

Structural Properties

HNT-Sn consist of nanoplates (Fig. 3a-3c) and HNT-Cn consist of nanoparticles (Fig 3d-3f) based on TEM images. HRTEM images taken from the edge of HNT-S1 and HNT-C1 reveal that the d-spacing between two consecutive planes are about 0.19 nm and 0.35 nm for HNT-S1 agreeing with the d_{200} and d_{101} values of anatase phase (Fig. 3g) and the distance between two consecutive planes is 0.35 nm for HNT-C1 agreeing with the d_{101} value of anatase phase (Fig. 3h). This reveals that HNT-S1 and HNT-C1 present different facets at crystal edges.

The structural properties of HNTs were studied using XRD technique. The peaks at 25.3°, 38.2°, 48.2°, 54.0°, 55.2°, 62.9°, 68.9° and 70.3° on the XRD patterns of HTN-S1-3 are indexed to (101), (004), (200), (105), (211), (204), (116) and (220) reflections of anatase phase (JCPDS 78-2486) as shown in Fig. 4a, which indicates that HNT-S1-3 consist of pure anatase phase. HNT-C1 contains pure anatase phase. However, HNT-C2, C3 contain dominant anatase phase with a little presence of rutile phase as evidenced by the minor peak at 27.5°, corresponding to the (110) reflection of rutile phase (JCPDS 78-1508) as seen in Fig. 4b. The data reveals that the chemical nature of acids plays an important role in the crystallization process.

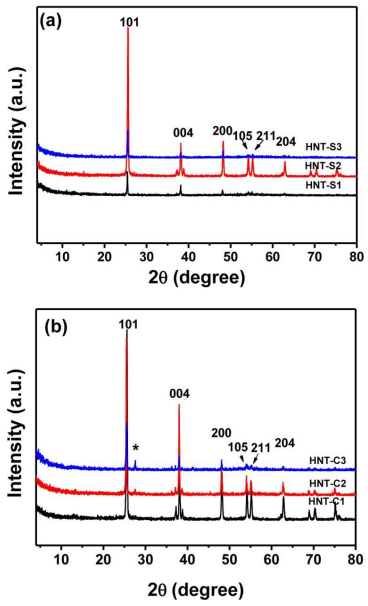

Fig.4 XRD patterns of the as-prepared hierarchically nanostructured TiO_2: (a) HNT-Sn; (b) HNT-Cn.

Growth Mechanism

The experimental data shows that the crystal morphology and structural properties of HNTs are affected due to the involvement of acids and the degree of which depends on the nature of acids used. Under hydrothermal conditions, acids, above a critical concentration, are capable to break the hydrogen bonds and

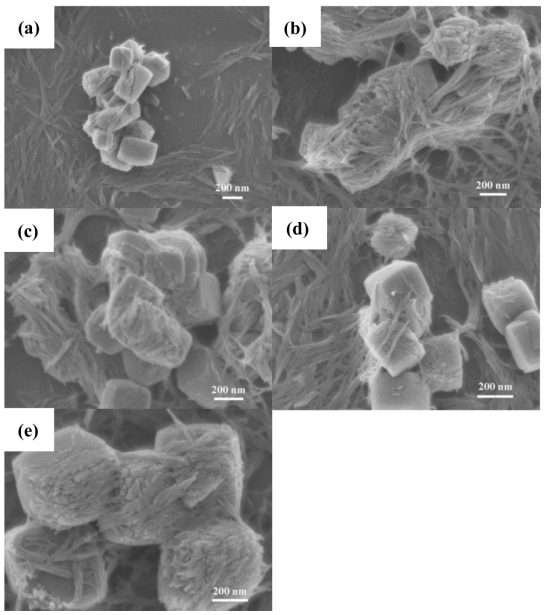

Fig.5 FE-SEM images of the HNTs coexisting with NCCs obtained at 120° by varying the amount of HCl.

penetrate into the noncrystalline and crystalline domains of cellulose, as a result, noncrystalline cellulose dissolve and NCC are partially esterified.[32] Depending on the type of acids used, NCC carries different surface functionalities and different negative charges, for example, esterification of one hydroxyl group of NCC using H_2SO_4 results in sulfate esters, which can capture the Ti^{4+} by coordination, and creates one negative charge.[32-33] We believe that the superficial functionalities and negative charges of cellulose play an important role in the growth of HNTs. The involvement of NCC carrying sulphonic acid group and more negative charge favors the growth of nanoplates by stabilizing the {002} facets of anatase and less negatively charged NCC without sulphonic acid group promotes the growth of nanoparticles. HNT-Cn products obtained from hydrothermal crystallization at 120°C are TiO_2/NCC composites as shown in Fig. 5, suggesting that NCC not only promotes the formation of nanostructures but also control the shape of TiO_2 nanocrystals. Thermogravimetric analysis (TGA) of HTNS1-3 shows a major weight-loss between 200°C and 800°C, giving solid residues of 83.0 wt%, 80.9 wt% and 75.1 wt%, respectively (Fig. S12 a-c). HNT-C1-3 also shows a major weight-loss between 200°C and 800°C, giving solid residues of 81.4 wt%, 84.1 wt% and 88.1 wt%, respectively (Fig. S12d-f), confirming the presence of carbonaceous materials. It has been generally established that rutile phase is preferentially grown from strong acidic medium under hydrothermal conditions and the phase transition is significantly affected by particle sizes.[36-37] However, this is not the case in the synthesis of HNTs involving NCC, as manifested by the crystallization of pure anatase phase in HCl-containing system at 140°C, dominant growth of anatase phase with a minor presence of rutile phase at 160°C and 180°C, and the formation of pure anatase phase in H_2SO_4-containing systems at 140°C-180°C. It is worth taking note that the surface texture of TiO_2 crystals become smooth with increasing acid-to-cellulose ratio, suggesting that thermodynamically more stable {101} facets start to evolve on crystal surface after the NCC wholly degraded (Fig. 1d).[35] It implies that NCC carrying sulphonic acid group and higher negative charges promotes the growth of pure anatase phase and the morphology of TiO_2 is determined by both the formation speed of TiO_2 and the dissociated speed of NCC as illustrated in Scheme 1.

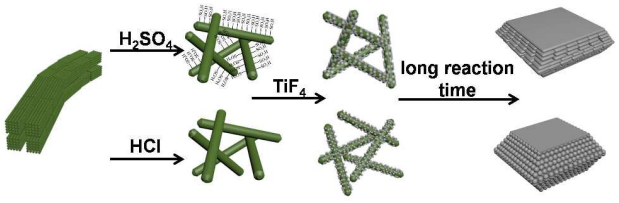

Scheme 1 A Schematic illustration of the formation of HNT-Sn and HNT-Cn in H_2SO_4 and HCl system, respectively.

Photocatalytic properties

The photocatalytic activity of the as-synthesized HNT-Sn and CHNT-Sn is evaluated by degradation of MO. As shown in Fig. 6a, the photocatalytic activity is in decreasing order of HTN-S3 > HTN-S1 > HTN-S2 and the photocatalytic activities of HNT-Sn are low. This could be due to the formation of partially coated crystal surfaces of TiO_2 by solid hydro-chars-insoluble carbonaceous materials during the hydrothermal synthesis of HNTs at range of 140°C-180°C. Such a coating retards the generation of excitons from TiO_2, excited by light, hence, reduces photocatalytic activity.[36-39]

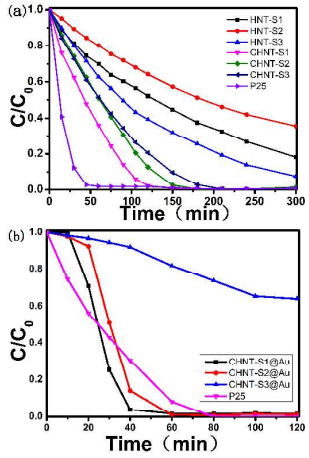

Fig.6 Photocatalytic degradation of MO in the presence of different photocatalysts: (a) CHNT-Sn and HNT-Sn; (b) CHNT-Sn@Au.

Calcination of HNT-Sn at 550°C removes carbonaceous coating, giving rise to CHNT-Sn. CHNT-S1, S2 contains pure anatase phase (Fig. S13). However, CHTN- S3 contain dominant anatase phase with a little presence impure phase, indicating that calcination can cause slight phase transition. Intriguingly, they exhibit greater photocatalytic activity than HNT-Sn, in the order of CHNT-S1 > CHNT-S2 > CHNT-S3, which differs from that of HNT-Sn, albeit they have lower photoactivity than P25. The improvement in photocatalytic activities is likely attributed to the removal of carbonaceous layer.

It is well established that the photocatalytic properties strongly depend on the crystallinity, specific surface character, light absorption, recombination rate of photogenerated hole-electron pairs, and so on.[40-50] To explain the observed photocatalytic activity, X-ray photoelectron spectra (XPS) was used to characterize the chemical nature of CHNT-Sn. The individual fitted XPS of C-1s, O-1s, S-2p and Ti-2p of CHNT-S1-3 are shown in Fig. S14. The XPS of C-1s exhibits a unique doublet with bonding energy of 284.7 eV and 288.7 eV (Fig. S14 a-c), which may be attributed to the adsorbed amorphous carbon, and carboxyl carbon, respectively.[51, 52] The O-1s peak presents a triplet with bonding energy of 530.5 eV and 531.9 eV (Fig. S14 d-f), which correspond to the lattice oxygen (O1) and O-C (O2), respectively.[52, 53] The Ti-2p peak is a unique doublet at around 459.4 eV-465.2 eV (Fig. S14 g-i), which is typical of Ti^{4+} in an octahedral environment.[52, 54] The S-2p peak is a singlet at around 168.7 eV (Fig. S14 j-l), which is typical of the S^{+6} of bidentate sulfate ions on the surface of CHNT-Sn.[55] Among the CHNT-Sn, CHNT-S1 exhibits the highest photocatalytic activity probably due to more S element (2.03 wt%) on the surface comparing to CHNT-S2 (1.66 wt%) and CHNT-S3 (1.81 wt%), which is helpful to improve the photocatalytic activity.[55] The CHNT-Cn and HNT-Cn show the similar photocatalytic activity as the CHNT-Sn and HNT-Sn as shown in Fig. S15.

Noble metel-TiO_2 heterostructure photocatalysts have attracted more attention owing to the localized surface plasmon resonance (LSPR) and the effective charge carrier seperation by forming a schottky barrier at the metal/TiO_2 interface.[56-59] The CHTN-Sn@Au heterostructures have been obtained by loading Au nanoparticles on the surface of CHTN-Sn. However, they show the different photocatalytic activity as shown in Fig. 6b. The degradation was obviously enhanced in the presence of CHNT-S1, S2@Au, larger than CHNT-Sn and P25 under the same experimental conditions. However, CHNT-S3@Au exhibits

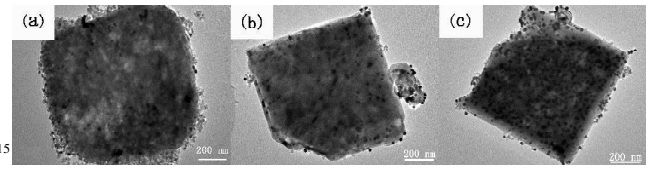

Fig.7 TEM images of the CHNT-Sn@Au: (a) CHNT-S1@Au; (b) CHNT-S2@Au; (c) CHNT-S3@Au.

very low photocatalytic activity. The XPS spectra show that a unique doublet with bonding energy of 83.3 eV and 86.9 eV for CHNT-Sn@Au, which can be attributed to the values for the Au $4f_{7/2}$ and Au $4f_{5/2}$ of metallic Au, respectively, (Fig. S16 a-c). It exhibits that CHNT-Sn@Au contain metallic Au nanostructure on the surface of CHNT-Sn. In general, the introduction of Au nanoparticle onto the TiO_2 can gradually improve the photocatalytic activity until the loading amount of Au nanopaticle reaches the optimal value. The further loading of Au nanoparticle will drastically decrease the photocatalytic activity.[60] It can be attributed to the following factors: (1) high loading will cover the surface active sites of TiO_2 and prohibit its contact with organic dye; (2) excessive loading of Au nanoparticle on the surface of TiO_2 should decrease the light adsoption and generation of photogenerated carriers; (3) Au nanoparticle with high loading amount can become recombination centers and lead to the decrease of photocatalytic activity. TEM images further indicate that the CHNT-S3@Au contains more Au nanopartices than the CHNT-S1@Au and CHNT-S2@Au, confirming that the lowest photocatalytic activity originates from the excessive Au loading amount for CHNT-S3@Au. The UV-vis absorption spectra further exhibit that CHNT-S3@Au showes the lowest adsoption among the CHNT-Sn@Au (Fig. 8), indicating that excessive loading of Au nanoparticle will increase the recombination center on the surface of TiO_2, leading to the decrease of photocatalytic activity.

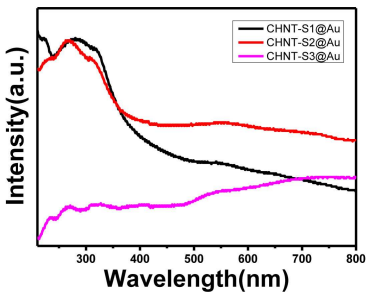

Fig. 8 UV-vis spectra of CHNT-Sn@Au.

Conclusions

This work reports an one-pot biotemplated hydrothermal approach to synthesize HNTs with different crystal morphology by using different acids and varying amount of MCC. We show that H_2SO_4 and HCl are capable of depolymerizing MCC above 120°C, forming NCC with different surface functionalities and surface charges that controls the formation of HNTs. Calcination of HNTs to remove surface carbonaceous species from TiO_2 crystals and loading Au nanoparticle on the CHNT-Sn will obviously improve their photocatalytic activities. The bio-templated synthetic approach offers an effective method to engineer inorganic crystals for enhanced functional performance.

Acknowledgements

The authors are grateful to National Natural Science Foundation of China for financial support (20971051) and Prof. T.F, Xie for the photocatalystic test and technical discussions.

Notes and references

State Key Lab of Inorganic Synthesis and Preparative Chemistry, Jilin University, 2699 Qianjin Street, Changchun 130012,P. R. China. Tel: 8643185167482; Email:wangyu@jlu.edu.cn.

† Electronic Supplementary Information (ESI) available: [details of any supplementary information available should be included here]. see DOI:10.1039/b000000x/†

1 W. D. Shi, S. Y. Song, H. J. Zhang, Chem. Soc. Rev., 2013, **42**, 5714-5743.
2 J. Schneider, M. Matsuoka, M. Takeuchi, J. Zhang, Y. Horiuchi, M. Anpo, D. W. Bahnemann, Chem. Rev., 2014, 114, 9919-9986.
3 L. Q. Liu, S. X. Ouyang, J. H. Ye, Angew. Chem. Int. Ed. 2013, 52, 6689-6693.
4 A. Fujishima, K. Honda, Nature, 1972, 238, 37-38.
5 Z. G. Xiong, X. S. Zhao, J. Mater. Chem. A, 2013, 1, 4403-4414.
6 J. Zhu, J. G. Wang, F. J. Lv, S. X. Xiao, C. Nuckolls, H. X. Li, J. Am. Chem. Soc. 2013, 135, 4719-4721.
7 Z. C. Lai, F. Peng, H. J. Wang, H. Yu, S. Q. Zhang, H. J. Zhao, J. Mater. Chem. A, 2013, 1, 4182-4185.
8 X. F. Yang, J. Chen, L. Gong, M. M. Wu, J. C. Yu, J. Am. Chem. Soc. 2009, 131, 12048-12049.
9 H. Q. Zhan, X. F.Yang, C. M. Wang, C. L. Liang, M. M. Wu, J. Phys. Chem. C 2010, 114, 14461-14466.
10 X. Y. Pan, M. Q. Yang, X. Z. Fu, N. Zhang, Y. J. Xu, Nanoscale, 2013, 5, 3601-3614.
11 K. Zhu, N. R. Neale, A. Miedaner, A. J. Frank, Nano Lett., 2007, 7, 69.
12 P. R. Liu, H. M. Zhang, H. W. Liu, Y. Wang, X. D. Yao, G. S. Zhu, S. Q. Zhang, H. J. Zhao, J. Am. Chem. Soc. 2011, 133, 19032-19035.
13 N. Roy, Y. K. Sohn, D. Pradhan, ACS Nano 2013, 7, 2532-2540.
14 B. Wang, L. J. Guo, M. He, T. Ye, Phys. Chem. Chem. Phys., 2013, 15, 9891-9898.
15 J. Y. Cao, Y. J. Zhang, L. Q. Liu, J. H. Ye, Chem. Commun., 2013, 49, 3440-3442.
16 G. Liu, H. G. Yang, J. Pan, Y. Q. Yang, G. Q. Lu, H. M. Cheng, Chem. Rev., 2014, 114, 9559-9612.
17 A. S. Barnard, L. A. Curtiss, Nano Lett., 2005, 5, 1261-1266.
18 S. Ponja, S. Sathasivam, N. Chadwick, A. Kafizas, S. M. Bawaked, A. Y. Obaid, S. A. Thabaiti, S. N. Basahel, I. P. Parkin, C. J. Carmalt, J. Mater. Chem. A, 2013, 1, 6271-6278.
19 G. H. Zhang, H. G. Duan, B. G. Lu, Z. Xu, Nanoscale, 2013, 5, 5801-5808.
20 Y. Yu, Z. M. Zhou, W.. Wen, Y. D. Zhao, RSC Adv., 2013, 3, 4880-4884.
21 J. M. Galloway, J. P. Bramble, S. S. Staniland, Chem. Eur. J. 2013, 19, 8710-8725.

22 B. Wicklein, G. S. Alvarez, J. Mater. Chem. A, 2013, 1, 5469-5478.
23 C. C. Hire, H. C. Genuino, S. L. Suib, D. H. Adamson, Chem. Mater. 2013, 25, 2056-2063.
24 M. M. Khan, S. A. Ansari, M. I. Amal, J. Lee, M. H. Cho, Nanoscale, 2013, 5, 4427-4435.
25 N. H. Munro, D. W. Green, K. M. McGrath, Chem. Commun., 2013, 49, 3407-3409.
26 G. Xiao, X. Huang, X. P. Liao, B. Shi, J. Phys. Chem. C 2013, 117, 9739-9746.
27 Z. J. Shi, G. O. Phillips, G. Yang, Nanoscale, 2013, 5, 3194-3201.
28 J. Q. Han, C. J. Zhou, Y. Q. Wu, F. Y. Liu, Q. L. Wu, Biomacromolecules 2013, 14, 1529-1540.
29 H. M. A. Ehmann, S. Spirk, A. Doliška, T. Mohan, W. Gössler, V. Ribitsch, M. S. Smole, K. S. Kleinschek, Langmuir 2013, 29, 3740-3748.
30 N. T. Cervin, L. Andersson, J. B. S. Ng, P. Olin, L. Bergström, L. Wågberg, Biomacromolecules 2013, 14, 503-511.
31 H. L. Zhu, S. Parvinian, C. Preston, O. Vaaland, Z. C. Ruan, L. B. Hu, Nanoscale, 2013, 5, 3787-3792.
32 S. C. Espinosa, T. Kuhnt, E. J. Foster, C. Weder, Biomacromolecules 2013, 14, 1223-1230.
33 H. Y. Yu, Z. Y. Qin, B. L. Liang, N. Liu, Z. Zhou, L. Chen, J. Mater. Chem. A, 2013, 1, 3938-3944.
34 S. Duri, C. D. Tran, Langmuir 2013, 29, 5037-5049.
35 M. Möller, F. Harnisch, U. Schröder, RSC Adv., 2013, 3, 11035-11044.
36 L. Pan, J. J. Zou, S. B. Wang, Z. F. Huang, A. Yu, L. Wang, X. W. Zhang, Chem. Commun., 2013, 49, 6593-6595.
37 G. W. Cui, W. L. Wang, M. Y. Ma, M. Zhang, X. Y. Xia, F. Y. Han, X. F. Shi, Y. Q. Zhao, Y. B. Dong, B. Tang, Chem. Commun., 2013, 49, 6415-6417.
38 C. Lin, Y. Song, L. X. Cao, S. W. Chen, Nanoscale, 2013, 5, 4986-4992.
39 J. Zhou, P. Lin, J. J. Ma, X. Y. Shan, H. Feng, C. C. Chen, J. R. Chen, Z. S. Qian, RSC Adv., 2013, 3, 9625-9628.
40 Z. C. Lai, F. Peng, H. J. Wang, H. Yu, S. Q. Zhang, H. J. Zhao, J. Mater. Chem. A, 2013, 1, 4182-4185.
41 K. Sabyrov, N. D. Burrows, R. L. Penn, Chem. Mater. 2013, 25, 1408-1415.
42 A. Li, Y. H. Jin, D. Muggli, D. T. Pierce, H. Aranwela, G. K. Marasinghe, T. Knutson, G. Brockman, J. X. Zhao, Nanoscale, 2013, 5, 5854-5862.
43 X. Y. Wu, S. Yin, Q. Dong, C. S. Guo, T. Kimura, J. I. Matsushita, T. Sato, J. Phys. Chem. C 2013, 117, 8345-8352.
44 Y. Wang, H. M. Zhang, P. Liu, X. D. Yao, H. J. Zhao, RSC Adv., 2013, 3, 8777-8782.
45 Q. Kang, J. Y. Cao, Y. J. Zhang, L. Q. Liu, H. Xu, J. H. Ye, J. Mater. Chem. A, 2013, 1, 5766-5774.
46 P. Goswami, J. N. Ganguli, RSC Adv., 2013, 3, 8878-8888.
47 H. Y. Zhang, Y. F. Zhao, S. Chen, B. Yu, J. L. Xu, H. J. Xu, L. D. Hao, Z. M. Liu, J. Mater. Chem. A, 2013, 1, 6138-6144.
48 S. Pany, K. M. Parida, B. Naik, RSC Adv., 2013, 3, 4976-4984.
49 A. Boonchun, N. Umezawa, T. Ohno, S. X. Ouyang, J. H. Ye, J. Mater. Chem. A, 2013, 1, 6664-6669.
50 B. Santara, P. K. Goro, K. Imakita, M. Fujii, Nanoscale, 2013, 5, 5476-5488.
51 F. Zhang, H. Cao, D. Yue, J. Zhang, M. Qu, Inorg. Chem. 2012, 51, 9544-9551.
52 C. D. Wagner, W. M. Riggs, L. E. Davis, J. F. Moulder, G. E. Muilenberg, Handbook of X-Ray Photoelectron Spectroscopy: a reference book of standard data for use in x-ray photoelectron spectroscopy, Perkin-Elmer MN, Eden-prairie, 1979.
53 J. Q. Yan, G. J. Wu, N. J. Guan, L. D. Li, Z. X. Li, X. Z. Cao, Phys. Chem. Chem. Phys., 2013, 15, 10978-10988.
54 A. Iwabuchi, C. Choo, K. Tanaka, J. Phys. Chem. B, 2004, 108, 10863-10871.
55 S. Pany, K. M. Parida, B. Naik, RSC Adv., 2013, 3, 4976-4984.
56 Z. Xiong, L. Zhang, X. S. Zhao, Chem. Eur. J., 2014, 14715-14720.
57 X. F. Wu, H. Y. Song, J. M. Yoon, Y. T. Yu, Y. F. Chen, Langmuir, 2009, 25, 6438.
58 Q. P. Lu, Z. D. Lu, Y. Z. Lu, L. F. Lv, Y. Ning, H. X. Yu, Y. B. Hou, Y. D. Yin, Nano Lett., 2013, 13, 5698-5702.
59 C. G. Silva, R. Juarez, T. Marino, R. Molinari, H. Garcia, J. Am. Chem. Soc. 2011, 133, 595-602.
60 R. B. Jiang, B. X. Li, C. H. Fang, J. F. Wang, Adv. Mater., 2014, 26, 5274-5309.